CHEMISTRY OF MATERIALS

pubs.acs.org/cm

Article

Cation Exchange during the Synthesis of Colloidal Type-II ZnSe-Dot/CdS-Rod Nanocrystals

Jannik Rebmann, Hans Werners, Florian Johst, Marcel Dohrmann, Yannic U. Staechelin, Christian Strelow, Alf Mews,* and Tobias Kipp*

Cite This: *Chem. Mater.* 2023, 35, 1238−1248

Read Online

ACCESS | Metrics & More | Article Recommendations | Supporting Information

ABSTRACT: Cation exchange is known to occur during the synthesis of colloidal semiconductor heteronanoparticles, affecting their band gap and thus altering their optoelectronic properties. It is often neglected, especially when anisotropic heterostructures are discussed. We present a study on the role of cation exchange inevitably occurring during the growth of anisotropic dot-in-rod structures consisting of a spherical ZnSe core enclosed by a rod-shaped CdS shell. The material combination exhibits a type-II band alignment. Two reactions are compared: the shell-growth reaction of CdS on ZnSe and an exchange-only reaction of ZnSe cores to CdSe. Transmission electron microscopy and a comprehensive set of optical spectroscopy data, including linear and time-resolved absorption and fluorescence data, prove that cation exchange from ZnSe to CdSe is the dominant process in the initial stages of the shell-growth reaction. The degree of cation exchange before significant shell growth starts was determined to be about 50%, highlighting the importance of cation exchange during the heteronanostructure growth.

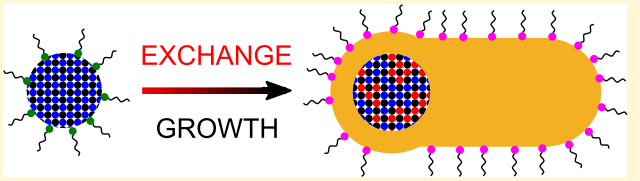

INTRODUCTION

Colloidal semiconductor heteronanostructures have great potential for optoelectronic devices because of their high quantum yields (QYs), tunable emission wavelengths, and variable fluorescence lifetimes.[1−7] In a classical core/shell nanostructure with a type-I band alignment, the larger band gap of the shell enclosures the smaller band gap of the core and thus passivates the core.[8−10] In a type-II nanostructure, the conduction band (CB) and valence band (VB) are staggered, which leads to a spatial separation of electrons and holes above the heterointerface. This results in large Stokes shifts,[11−13] long fluorescence lifetimes,[14,15] and the fluorescence switchability upon external stimuli like external fields.[16−19] Moreover, type-II heterostructures are of great interest for photocatalysis because of their intrinsic property to spatially separate photoexcited charge carriers.[15,20,21]

The material system ZnSe/CdS exhibits a type-II band alignment, as sketched in Figure 1a. It has been shown to be suitable for the synthesis of heteronanostructures of different shapes, like spherical core−shell nanocrystals,[22,23] tetrapods,[24] dumbbells,[25] or dot-in-rod structures.[14,16] Since in this system, both materials consist of different cations, cation exchange can occur during the nanostructure synthesis. In fact, ZnSe and CdSe are fully miscible and are known to be exchangable.[26−28]

For spherical ZnSe-core/CdS-shell nanocrystals, Boldt et al. showed how the optical properties can be adjusted by controlled interdiffusion of cations across the heterointerface.[22,23] Compared to spherical structures, anisotropic ZnSe-dot/CdS-rod nanostructures exhibit additional degrees of freedom for designing their optical properties due to the expanded delocalization of charge carriers. Since the synthesis of a rod-like CdS shell around a ZnSe core is typically performed in an excess of Cd ions, these can partially exchange Zn ions such that $Zn_{1-x}Cd_xSe$ cores are formed. Since CdSe/

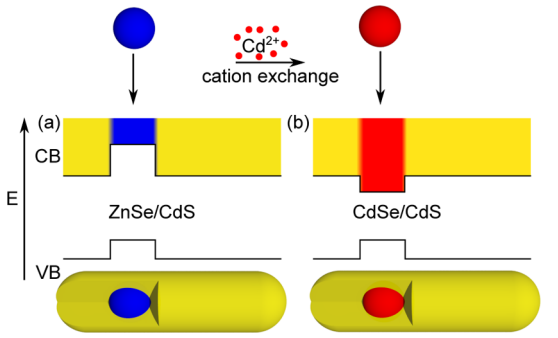

Figure 1. Schematic band alignment of (a) ZnSe/CdS and (b) CdSe/CdS dot-in-rod nanostructures. The offset of the conduction band is lowered when Zn^{2+} ions are exchanged by Cd^{2+} ions. This changes the band alignment from type-II to type-I.

Received: October 30, 2022
Revised: December 13, 2022
Published: January 31, 2023

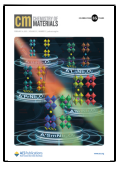

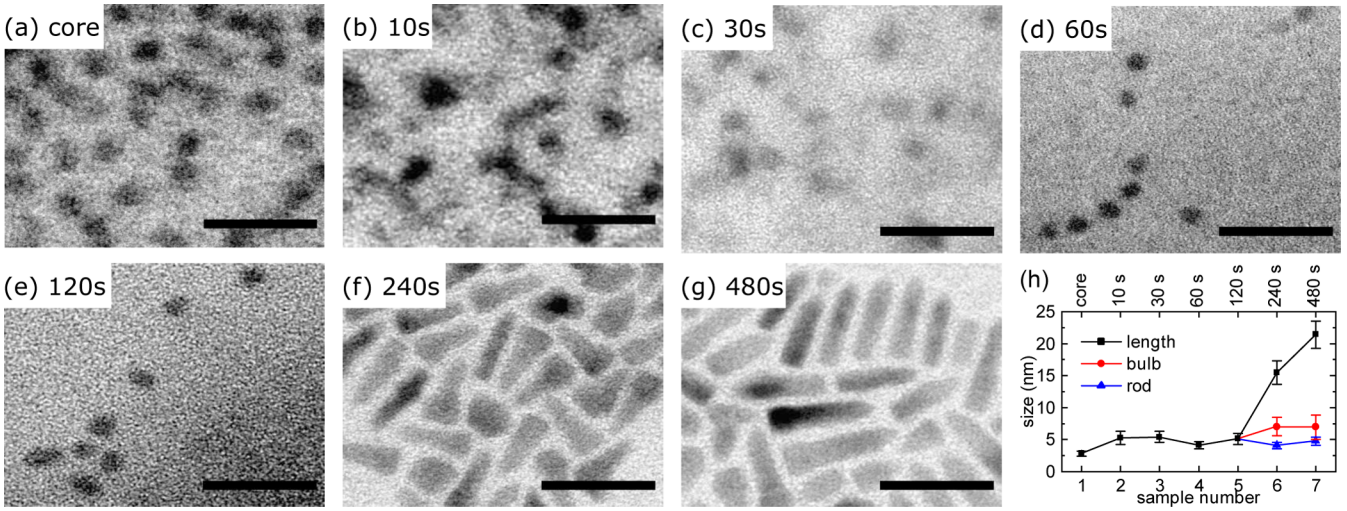

Figure 2. (a–g) Representative TEM images of (a) ZnSe core sample and (b–g) aliquots of the growth series, belonging to reaction times as noted. Scale bars: 25 nm. (h) Sizes of the length, rod diameter, and bulb diameter (if distinguishable) as determined by TEM vs the sample number. Lines connecting data points are guides to the eye.

CdS exhibits a type-I band alignment, as depicted in Figure 1b, the successive exchange of ZnSe to CdSe in the core material eventually leads to a transition from a type-II structure to a type-I structure. During cation exchange in particular, the conduction band edge is lowered, as sketched in Figure 1. Therefore, understanding the growth mechanism and the role of cation exchange in the synthesis of ZnSe/CdS dot-in-rod structures is not only of fundamental interest but also needed to tailor the optoelectronic properties of such heterostructures.

A major step in this direction was performed by Dorfs et al., who directly coated ZnSe cores with the anisotropic CdS shell. They observed that the shell growth is slow in the first 40 s of reaction time but increases thereafter so that the complete rod-shaped shell is formed after 120 s. The realization of type-II heterostructures was proven based on spectroscopic data, but the possibility of cation exchange in the core material was not taken into account.[14,29]

In a different work, Hewa-Kasakarage et al. first coated spherical ZnSe cores with two to three monolayers of a spherical CdS shell before an anisotropic CdS shell was grown. The growth process was monitored, but cation exchange or interdiffusion was not addressed.[16]

In this work, we investigate the synthesis of ZnSe/CdS dot-in-rod nanostructures in particular with respect to the cation exchange. We monitored the growth of an anisotropic CdS shell on spherical ZnSe cores by taking aliquots at different reaction times to perform transmission electron microscopy (TEM) as well as steady-state and time-resolved UV/vis absorption and photoluminescence (PL) measurements. In addition, we performed control experiments in which only cation exchange can occur but the shell growth is inhibited. We find that cation exchange is indeed the dominant process in the beginning of the shell-growth reaction: about 50% of the initial Zn ions in the core are exchanged by Cd ions before a significant CdS shell has been formed during the reaction.

RESULTS AND DISCUSSION

Pairs of sample series are investigated, which consist of the so-called growth and exchange series, respectively. For each series, the starting point for the synthesis is pre-synthesized ZnSe core nanocrystals from the same batch dissolved and stored in trioctylphosphine (TOP). For the growth series, these ZnSe cores were dispersed in a mixture of sulfur and TOP (S/TOP) and hot-injected into a Cd precursor solution. The amount of the Cd precursor determines the CdS shell length. In our case, the ratio of Cd ions from the precursor to Zn ions from the ZnSe cores was 32:1. For the exchange series, the reaction conditions were absolutely identical except for using plain TOP instead of S/TOP. For both series, after certain reaction times between 10 s and 8 min, six samples were taken from the solutions for their later investigation. Thus, in the growth series, Cd and S were present in the reaction solution, allowing CdS to be formed, while in the exchange series, only Cd and no S was present.

Investigation by Transmission Electron Microscopy. Figure 2a–g shows representative TEM images of the original core sample and of aliquots of the growth series, from which changes in size and shape during the reaction time can be deduced. The ZnSe cores exhibit a spherical shape with a diameter of about 3 nm. The particles of the aliquots appear to be spherical in the early reaction, up to about 120 s of reaction time. After 240 s of reaction time, an anisotropic shape is evident. One end of the rod is thicker than the other and is presumably the location of the ZnSe core.[14]

Figure 2h summarizes the sizes of the particles at the different reaction stages as determined by TEM. Almost no increase of diameter occurs in the first 60 to 120 s of reaction time. The rod growth is observable only for longer reaction times, leading to a rod length of about 22 nm after 480 s of reaction time.

Even though the TEM images in Figure 2 are the best ones that were obtained during this study, the contrast is very weak. This is because of the organometallic cadmium phosphonate precursor, which is used as the cadmium source during the reaction. At early reaction stages, the unreacted cadmium precursor is still present in the samples. It is known that cadmium phosphonate forms polymeric layered structures.[30−32] This unreacted polymer precipitates in the cleaning procedure of the aliquots, when a polar solvent is added to precipitate the nanoparticles. Thus, the particles are trapped in the cadmium phosphonate polymer[33] and cannot be separated. The cadmium phosphonate complex shows low solubility and

https://doi.org/10.1021/acs.chemmater.2c03278
Chem. Mater. 2023, 35, 1238−1248

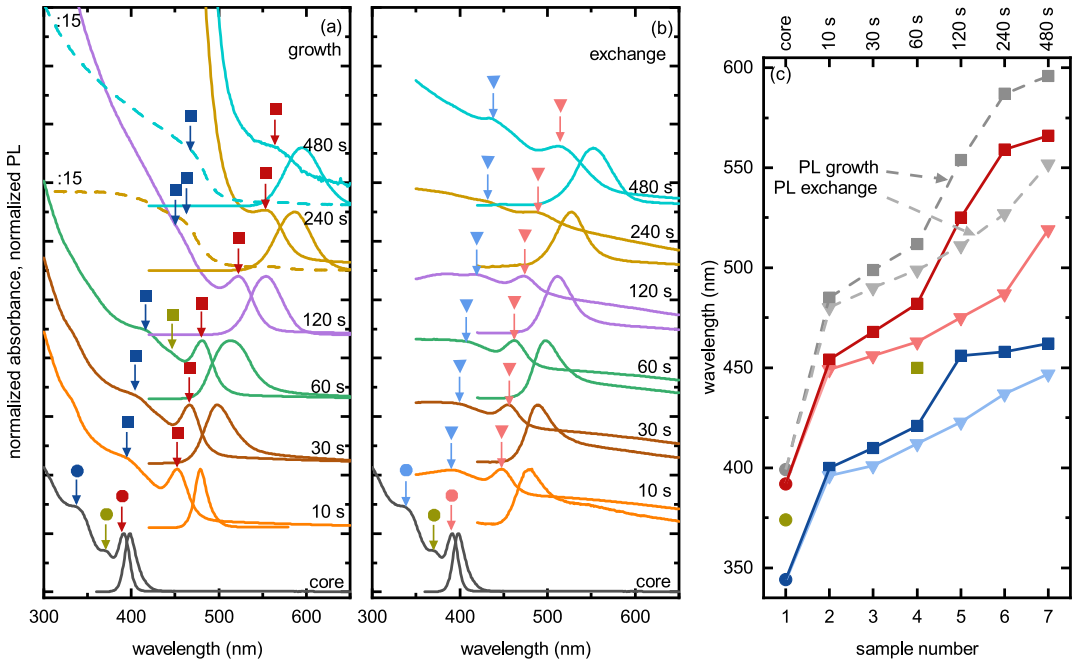

Figure 3. (a,b) Linear absorption and PL spectra of the (a) growth and (b) exchange sample series. Absorbance spectra are normalized to the first excitonic feature. Excitonic absorption maxima are marked with arrows and symbols. Dashed spectra correspond to the solid spectra of the same color divided by 15. (c) Position of all absorption and emission features marked in (a) for the growth series (squares) and (b) for the exchange series (triangles) vs the sample number. Lines connecting data points serve as guides to the eye.

melts only above 250 °C.[31,34] It produces high noise in TEM images and X-ray diffraction patterns, which hinders any further studies using high-resolution TEM, including high-resolution energy-dispersive X-ray spectroscopy, or X-ray diffraction.[30−34]

Hence, in the following, we present a detailed study of the changing optical properties of particles in solution to further investigate the different stages of the reaction.

Linear Absorption and PL Measurements. Figure 3 shows UV/vis absorption and PL spectra of all aliquots of (a) the growth series and (b) the exchange series. All spectra are normalized to their corresponding intensity of the low-energy transition.

The absorption spectrum of the core solution [given in panels (a) and (b)] shows the ground-state excitonic transition at a wavelength of about 392 nm (marked by a red arrow) as well as higher energy transitions at shorter wavelengths (marked by blue and dark yellow arrows). The PL emission is centered at about 399 nm; thus, the Stokes shift can be calculated to be 56 meV.

Regarding first the aliquots of the growth series (Figure 3a), the general shape of the UV/vis absorption spectra resembles that of the core spectrum with their features being continuously red-shifted until a reaction time of 60 s. After that, a strong absorption below 475 nm dominates the spectra, while the lowest excitonic transition at larger wavelengths (red arrows) remain visible as a shoulder. The PL emission is also shifting to the red with increasing reaction time. The Stokes shift abruptly increases already for the first aliquot to 175 meV and stays rather constant for longer reaction times. The red shift of the excitonic peaks both in absorption and emission cannot be explained by the growth of a CdS shell around the ZnSe core accompanied by a type-II band alignment between the core and shell material because according to TEM, no significant increase of particle diameter was observed for early aliquots. Hence, this suggests that this initial red shift is not caused by CdS growth but by cation exchange from ZnSe to CdSe. The increase of absorption below 475 nm for long reaction times could then be explained by the formation of CdS during the reaction (bulk band gap of CdS: 2.44 eV, corresponding to 500 nm).

To validate the assumption of the cation exchange being responsible for the red shift at early stages, samples from the exchange series were taken at the same reaction intervals and investigated by UV/vis absorption spectroscopy and PL spectroscopy. Corresponding spectra are shown in Figure 3b. Similar to the growth series, the lowest excitonic transition (red arrows) continuously shifts to the red with increasing reaction time. In addition, the PL peak also shifts to longer wavelengths, while the Stokes shift again stays nearly constant over the reaction time.

Since for the exchange series no sulfur precursor is present during the reaction, a CdS shell growth can be ruled out. Here, the cation exchange reaction from the original ZnSe core nanocrystals (bulk band gap of ZnSe: 2.73 eV) to intermixed $Zn_{1-x}Cd_xSe$ (bulk band gap of CdSe: 1.76 eV) can be the only reason for the observed red shift.

Figure 3c compares the position of all absorbance features marked by arrows in Figure 3a,b as well as the PL peaks of both the growth and exchange sample series. The horizontal axis gives the sample number, which is a non-linear representation of the reaction time. Noticeably, the excitonic ground-state absorption, a higher-state absorption, and the PL emission wavelength behave very similarly for both sample series up to a reaction time of about 60 s. Major differences of the absorption and emission wavelengths between growth and exchange series are only visible for reaction times longer than 60 s.

The similarity of absorption and emission wavelengths between the two series of samples for reaction times smaller 60

https://doi.org/10.1021/acs.chemmater.2c03278
Chem. Mater. 2023, 35, 1238−1248

s suggests that similar processes take place during their reactions. Since cation exchange from Zn to Cd is the only possible process that explains the observed red shift for the exchange series, this process seems to be dominant also in the early stages for the growth series. The difference in absorption and emission wavelengths for reaction times longer than 60 s reveals that a fundamentally different process occurs for the growth series as compared to that for the exchange series. We attribute this to the growth of a CdS shell around the core nanocrystals that were originally ZnSe and were (partially) cation-exchanged to $Zn_{1-x}Cd_xSe$ in the earlier course of the reaction.

Estimating the Degree of Cation Exchange. It is of importance to estimate the degree of cation exchange that occurred during the reactions as it determines the final CB and VB profiles. Hence, two independent methods were used to quantify the degree of cation exchange.

First, the composition of a final ZnSe-dot/CdS-rod sample after completed rod growth was determined by elemental analysis using inductively coupled plasma mass spectrometry (ICP−MS). Here, we determined the Zn to Se ratio since both ions are present in the initial ZnSe core and only Zn is partially exchanged to Cd. The ratio of Zn to Se in the final dot-in-rod structure was found to be 0.5:1. In comparison, pure ZnSe cores before rod growth show a ratio of Zn to Se of 1.2:1. Hence, about 50 to 60% of the Zn ions of the original ZnSe core nanocrystals are exchanged by Cd ions in the final dot-in-rod structure.

Second, the exciton energy for spherical $Zn_{1-x}Cd_xSe$ nanocrystals was calculated in dependence of x within the effective mass approximation including the direct Coulomb interaction. The Schrödinger and Poisson equations were numerically solved in an iterative way using the commercial software COMSOL Multiphysics, following the procedure reported by Panfil and co-workers.[35,36] Importantly, for the calculations, we assumed a spatially homogeneous alloy within the nanocrystals. This assumption is justified by the work of Groeneveld et al., who reported on homogeneous alloying of even slightly larger ZnSe nanocrystals in a Cd cation exchange reaction already at much lower reaction temperatures of 240 °C within 60 s of reaction time. It was demonstrated that the rate-limiting steps in the exchange reaction are the processes on the nanocrystal surface and not the diffusion of Cd ions within the crystal, resulting in a fast homogeneous distribution of cadmium and zinc ions at high temperatures.[26] Homogeneous alloying in cation-exchanged $Zn_{1-x}Cd_xSe$ nanocrystals has also been reported by Zhong and co-workers.[37] One might assume that lower temperatures during the synthesis lead to inhomogeneous alloying. However, we found that already at temperatures of 250 °C, no growth of the rod-like CdS shell occurs.

Figure 4 shows the calculated change in exciton energy ΔE of alloyed $Zn_{1-x}Cd_xSe$ nanocrystals for varying x compared to the exciton energy of pure ZnSe nanocrystals. For the calculation, a nanocrystal diameter of 3.16 nm was assumed, as estimated from the measured excitonic UV/vis absorption energy.[38] The calculations reveal that increasing the amount of Cd from pure ZnSe to pure CdSe in alloyed nanocrystals decreases the exciton energy by about 0.9 eV. This decrease would correspond to a red shift of the absorption and emission energies. The horizontal lines in Figure 4 represent experimental values of the red shifts after certain reaction times as determined from the emission spectra of the exchange

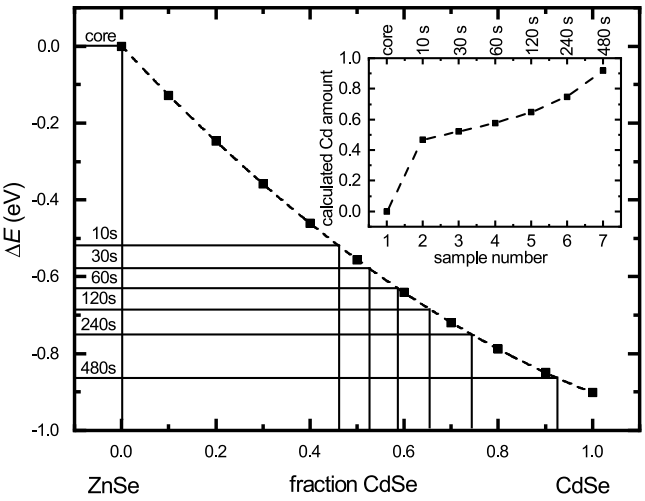

Figure 4. Calculated change in exciton energy of spherical $Zn_{1-x}Cd_xSe$ nanocrystals with respect to that of pure ZnSe nanocrystals. The dashed line represents a continuous fit for the discrete data points. Horizontal lines represent energy shifts as measured in PL experiments of the exchange sample series (cf. Figure 3b). Points of intersection with the fit function give values of the estimated amount of Cd within the respective nanocrystal sample. In the inset, the x determined in this way is plotted against the corresponding sample number.

series shown in Figure 3b. From their intersections with the dashed line, which connects calculated data points, corresponding values of x can be estimated. As summarized in the inset of Figure 4, x increases rapidly within the first seconds of the reaction. After 10 s, already roughly 45% of Zn is exchanged by Cd. After 30 s of the exchange reaction, x has increased to approximately 50%.

Both the estimated degree of cation exchange in the readily prepared dot-in-rod sample and the calculated degree of cation exchange coincide well under the assumption that cation exchange is the dominant process in the early stages of the growth reaction before CdS shell growth starts.

Growth Model for CdS on ZnSe Cores. Figure 5a−d illustrates the proposed reaction progression for both the growth sample series and the exchange sample series. The starting point for both sample series is spherical ZnSe core nanocrystals covered with octadecylamine (ODA) ligands (cf. Figure 5a). A solution of ZnSe cores with (growth series) or without (exchange series) the sulfur precursor is injected into a hot Cd precursor solution containing octadecylphosphonic acid (ODPA) and hexylphosphonic acid (HPA). For both sample series, it is assumed that a surface modification such as ligand exchange takes place early after injection, where the amines are replaced by the phosphonic acids (cf. Figure 5a,b).[27,39,40] Experimental evidence for this ligand exchange will be discussed later using data from time-resolved optical spectroscopy.

For the exchange series, the only possible process that can explain the observed red shift of the excitonic features is cation exchange from Zn to Cd since here the reaction solution does not contain any extra anions that could lead to a further growth of the nanocrystals, which would be accompanied by a decrease in quantum confinement. Comparison of the experimentally determined excitonic energy shifts to theoretical modeling suggests that already after 10 s of reaction time, about 45% of the Zn ions are exchanged by Cd (cf. Figure 4).

https://doi.org/10.1021/acs.chemmater.2c03278
Chem. Mater. 2023, 35, 1238−1248

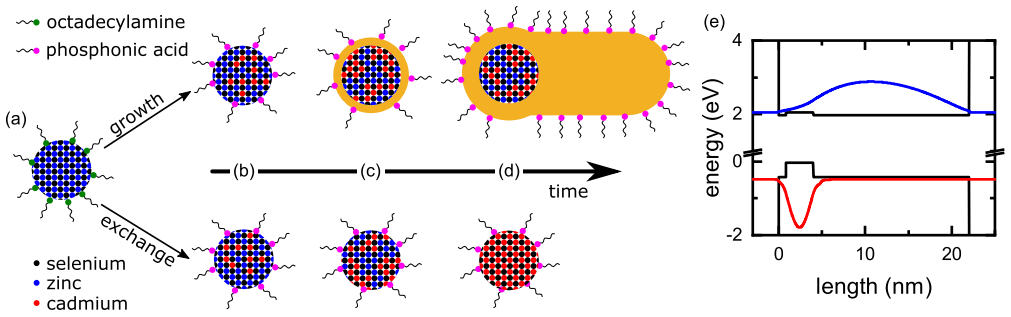

Figure 5. (a–d) Model for the comparison of growth of a CdS shell on ZnSe cores and exchange from ZnSe to CdSe. In the growth series, partial cation exchange from ZnSe to $Zn_{1-x}Cd_xSe$ is followed by CdS shell growth. In the exchange series, exchange of Cd into the ZnSe core leads to a nearly fully exchanged CdSe core. (e) Potential landscape (black) and single-particle wave functions of the electron (blue) and the hole (red) in a dot-in-rod structure with a partially exchanged $Zn_{1-x}Cd_xSe$ core with $x = 0.5$.

The degree of cation exchange is visualized in Figure 5 by partially changing the color representing the cations from blue to red. Since the ZnSe core nanocrystals are rather small and the reaction temperature is high, it is important to note that the exchanged Cd ions are expected to be homogeneously distributed even in the beginning of the reaction.[26,37]

In TEM images of the aliquots of the growth series at early reaction stages, no shell growth is evident. The great similarities in the linear absorption and PL spectra between the two sample series for early reaction times up to 60 s prove that in the beginning, cation exchange is the dominant process also for the growth series. Consequently, we assume that up to reaction times of 30 s to 60 s, the products of the growth series are essentially the same as those of the exchange series (cf. Figure 5b). The modeling for the exchange series delivered a degree of cation exchange of $x = 0.5$ after about 30 s of reaction time. Subtle red shifts of the absorbance and PL maxima of the growth series compared to that of the exchange series suggest slight passivation of the partially exchanged $Zn_{1-x}Cd_xSe$ core nanocrystals by CdS (cf. Figure 5c).

For reaction times of 60 s and larger, the positions of absorbance and PL features begin to diverge sharply between growth and exchange series. For the growth series, the pronounced red shifts of the lowest-energy excitonic features in PL and absorption are the result of CdS shell growth on partially exchanged $Zn_{1-x}Cd_xSe$ cores, drastically altering the quantum confinement within the nanostructures (cf. Figure 5c,d). With the formation of the complete shell, further cation exchange should be slowed down because the thermodynamically preferred composition of $Zn_{0.5}Cd_{0.5}Se$ has already been reached[23] and the higher stability of zinc phosphonate than that of cadmium phosphonate is not a driving force for exchange after shell deposition.[26] Results of the elemental analysis revealed a Zn/Se ratio of 0.5, which coincides well with the estimated x of the exchange series after about 30 s of reaction time. The growth of the CdS shell for long reaction times in the growth series is also evident by the increase of absorbance in the wavelength range of 475 nm (cf. Figure 3a), which corresponds to the CdS bulk band gap plus confinement energy, where the latter decreases for increasing reaction time.

It is striking that the CdS shell growth does not start directly upon injection of the ZnSe cores into the precursors. We attribute this to the higher reaction speed of the cation exchange reaction in the beginning than that of the shell growth. Cd ions are initially consumed for exchange until the exchange rate decreases due to the higher cadmium amount in the $Zn_{1-x}Cd_xSe$ core. Thus, the growth becomes more likely. Anisotropic growth of the shell is promoted by high reaction temperatures, which lead to the growth of CdS in the wurtzite phase. It is further supported by the combination of phosphonic acids as ligands that passivate unpolar side facets better than polar basal facets.[41]

For the exchange series, for reaction times larger than 60 s, an ongoing cation exchange reaction is assumed until ultimately the former ZnSe core nanocrystals have completely transformed to CdSe (cf. Figure 5d). A complete exchange can be expected after reaction times of several minutes (cf. Figure 4). It is worth noting that we observed degradation in the exchange series of different sample pairs for long reaction times. We attribute this to the rapid exchange from smaller Zn^{2+} to bigger Cd^{2+}, which might introduce defects.[26] The details are beyond the scope of this study as it is not the main process in early reaction stages.

Figure 5e shows the CB and VB profiles along the rod axis for the final dot-in-rod sample. It has been calculated assuming a partially exchanged homogeneous $Zn_{1-x}Cd_xSe$ core with $x = 0.5$, as determined by ICP–MS, surrounded by a CdS shell. The values for the effective masses, band gaps, and offsets were taken from refs 42 and 43. Further details can be found in Table S1. The potential landscape exhibits a clear type-II character with staggered bands. We calculated the single-particle electron and hole wave functions within such a potential assuming a core diameter of 3.16 nm, according to the initial ZnSe core size, and a shell geometry as obtained from TEM, that is, a length of 22 nm and a diameter of 4.77 nm (cf. Figure 2). Results are also shown in Figure 5e, illustrating the type-II-induced spatial charge separation, with the hole being localized in the core and the electron being delocalized within the shell. Calculations for dot-in-rod heterostructures with ZnSe and CdSe cores for comparison are shown in the Supporting Information.

In the following, we discriminate between type-II band alignment and type-II and quasi-type-II behavior. The band alignment is dependent on the composition of the core and shell materials, and the behavior is determined by the band alignment and the size of the core and shell. Particles with thin CdS shells exhibit type-II band alignment with the hole being confined in the core. The electron is being delocalized over the whole particle because it cannot be exclusively confined within a thin shell, which is ultimately referred to as quasi-type-II behavior. The type-II band alignment leads to a significantly decreased electron–hole overlap as soon as the shell thickness or length increases such that the electron effectively avoids the core region, which is called type-II behavior. As long as no

https://doi.org/10.1021/acs.chemmater.2c03278
Chem. Mater. 2023, 35, 1238–1248

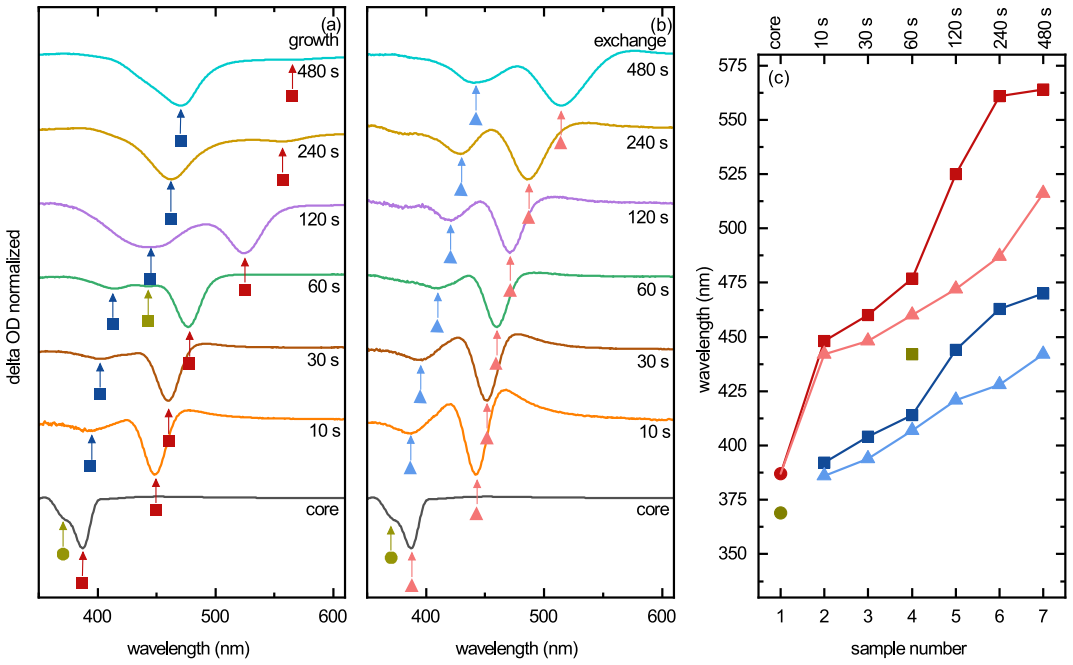

Figure 6. (a,b) TA spectra of the (a) growth and (b) exchange series. All spectra are normalized to their feature exhibiting the strongest bleach, respectively. The spectra correspond to pump−probe delay times between 1 and 3 ps, where the ground-state exciton transition reaches its maximum bleach. The absorption features are marked with arrows and symbols. All samples were excited with a wavelength of 330 nm ± 20 nm. (c) Position of TA bleach features marked in (a) for the growth series (squares) and (b) for the exchange series (triangles) vs the sample number. Connecting lines are guides to the eye.

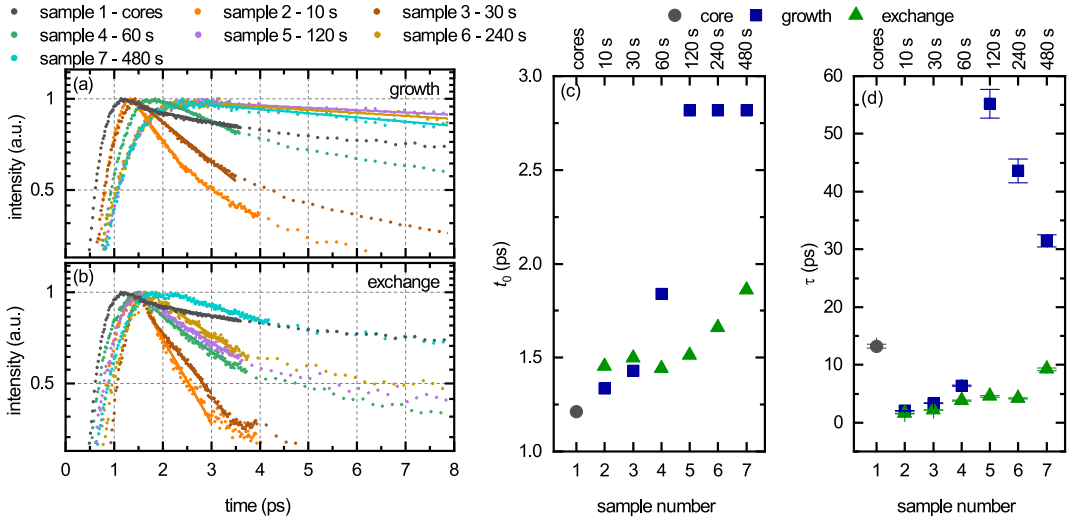

Figure 7. (a,b) TA dynamics at the position of the ground-state exciton (red arrows Figure 6a,b for samples of the (a) growth and (b) exchange series. Symbols represent measured data, and solid lines represent the monoexponential fits. (c) Rise time t_0 and (d) decay time τ vs the sample number extracted from (a) and (b) for the growth (blue squares) and exchange (green triangles) series.

shell growth occurs, no kind of band alignment can be assigned to the alloyed core-only particles.

Time-Dependent Optical Spectroscopy. Time-dependent optical spectroscopy was performed to work out differences in the exciton dynamics during cation exchange and subsequent growth of the elongated CdS shell. It gives insights into the charge carrier separation due to the type-II band alignment of the final sample as well as of late reaction stages. Transient absorption (TA) spectroscopy is able to resolve ultrafast exciton dynamics in the picosecond regime, whereas exciton dynamics on the nano- to microsecond timescale are addressed by fluorescence lifetime measurements.

Transient Absorption Spectroscopy. TA measurements were performed with a pump wavelength of 330 nm ± 20 nm, which leads to an excitation far above the band gap of the core particles. We used a constant and rather high pump fluence to compensate for small absorption cross-sections of early particles and to achieve acceptable signal-to-noise ratios that are decreased by scattering on cadmium phosphonate polymeric impurities, as already mentioned above. Further details are given in the Experimental Section.

Figure 6 shows normalized TA spectra of all samples of (a) the growth series and (b) the exchange series. The spectra correspond to pump−probe delay times between 1 and 3 ps,

https://doi.org/10.1021/acs.chemmater.2c03278
Chem. Mater. 2023, 35, 1238−1248

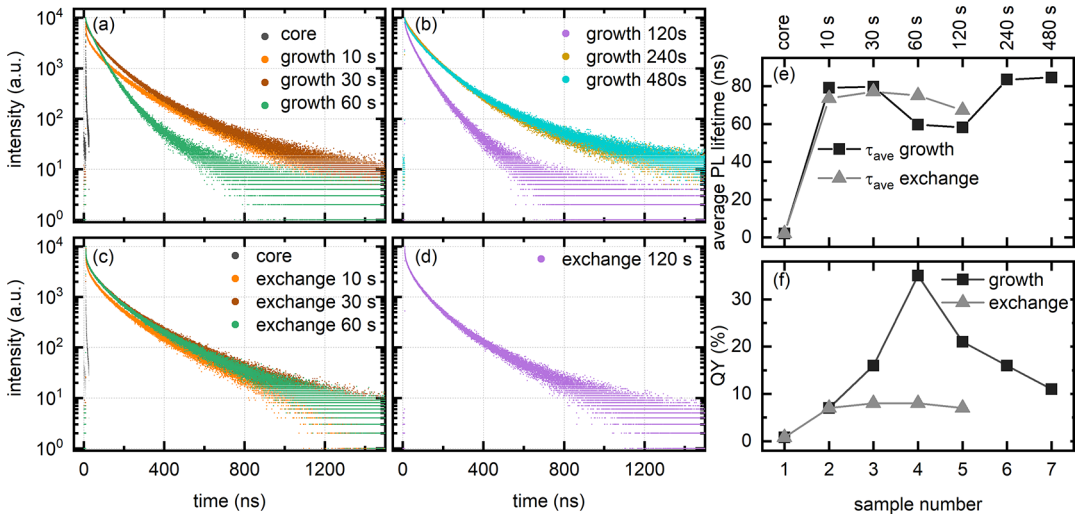

Figure 8. (a−d) Fluorescence decay curves of pure ZnSe cores, growth series (a,b), and exchange series (c,d). All samples were excited above the CdS band gap energy, with the repetition rates of 3.7 MHz (ZnSe cores) and 0.59 MHz (all aliquots), respectively. (e,f) Comparison of growth and exchange series regarding the (e) average lifetimes of the decay curves and (f) QY of each sample, measured in relation to the organic dye Coumarin 153. Lines are guides to the eye.

where the respective ground-state exciton transition (marked by red arrows) reaches its maximum bleach. All spectra are normalized to their feature exhibiting the strongest bleach, respectively.

Generally, the features that are observed in the linear absorption data in Figure 3a,b can also be seen in the TA spectra. The TA spectra better allow us to identify higher-state exciton transitions in particular for samples belonging to long reaction times, for which the UV/vis spectra are masked by scattering and detector saturation.

Figure 6c compares the position of all TA features marked by arrows in Figure 6a,b of both the growth and exchange sample series. Like in Figure 3c for the linear absorption, for reaction times up to 60 s, the TA bleaches occur at similar wavelengths for both sample series.

Starting at roughly 60 s, distinct differences occur. The energy needed to excite the ground-state exciton for the growth series shifts more strongly to the red than for the exchange series. Additionally, for the growth series, a more complex signature in the bleach signals of higher-state transitions occurs, best visible in the spectrum of the 60 s sample (marked dark blue and dark yellow).

In contrast, the exchange series exhibits only one higher-state transition bleach signal in the corresponding wavelength regime (light-blue triangles), which red-shifts similarly to the ground-state exciton transition bleach of the exchange series. Overall, also, the TA spectra reveal that the reaction processes in both sample series are similar for short reaction times, before the CdS shell growth starts after about 60 s of reaction time.

Figure 7a,b shows the picosecond TA dynamics at the position of the ground-state exciton (red arrows Figure 6a,b) for samples of the growth and exchange series, respectively.

In the following, two parameters that describe the transients are discussed: (i) the time required to reach the maximum bleach, here called the rise time t_0 and (ii) the decay time τ of the fastest dynamic, determined by fitting a monoexponential decay that starts shortly after the intensity maximum to avoid artifacts from the liquid-phase sample.[44] Details are given in the Supporting Information.

In Figure 7c, t_0 values for the growth (blue squares) and exchange (green triangles) series are given versus the sample number. The rise time is the shortest for the core sample and tendentially increases with the sample number, that is, reaction time. For reaction times up to 60 s, t_0 behaves similarly for both sample series. For a reaction time of 60 to 120 s, t_0 drastically increases for the growth series, while it only slowly increases for the exchange series. The general increase in rise time with increasing reaction time seen in the exchange series and in early samples of the growth series is congruent to the previously discussed red shifts of the ground-state exciton transition energies during the cation exchange. Since the TA experiment was conducted with constant pump power and, more important, constant pump energy, the relaxation time to the probed ground-state increases for every sample.[45] The strong increase of t_0 for the growth series can be explained with the growth of a shell during the reaction. Due to shell growth, type-II band alignment is achieved. With increasing shell thickness or length, the behavior changes from quasi-type-II to type-II. Photoexcited charge carriers need to separate across the interface of the core−shell structure and relax down to the ground-state exciton, which increases the rise time.

Figure 7d shows the decay times τ versus the sample number, determined for the growth (blue squares) and the exchange (green triangles) series. The decay time τ as analyzed here represents very fast multi-exciton decay channels, which are governed by Auger recombinations. There is a considerable shortening of τ between the core sample and the first aliquots of both series, which is most likely caused by surface modification upon injection of the cores into an excess of phosphonic acid ligands and Cd ions[46,47] (cf. Figure 5a,b).

The most prominent feature of the data is the strong increase of τ at a reaction time of 120 s only within the growth series. The increase can be explained with the initial growth of the CdS shell and its transitioning into a rod-like shape on the core nanocrystal. For nanoscaled systems it has been shown that the increase in volume reduces the Auger recombination rate.[48−52] Here in particular, the emerging type-II behavior results in a lower wave function overlap, additionally reducing the Auger rate. For longer reaction times, the decay time τ

https://doi.org/10.1021/acs.chemmater.2c03278
Chem. Mater. 2023, 35, 1238−1248

slightly decreases. This might be explained by the fact that as the length of the rod-shaped shell of the nanocrystal increases, not only the absorption but also the possibility of charge carrier trapping at the rod surface increases.[3,21,53] Charge carrier trapping and trap-assisted Auger recombination have been shown to decrease the Auger lifetime of the ground-state bleach.[47,54−57]

Fluorescence Lifetimes and Quantum Yield. Figure 8a−d shows fluorescence decay curves, which were measured on a second pair of sample series with a slightly smaller core size (see the Supporting Information for details of the sample set and the Experimental section for details of the measurement).

The decay for the ZnSe core sample is much faster than for all other samples of both the growth and exchange series. The main reason for this must be the different surface composition of the ZnSe core nanocrystals compared to that of aliquot samples of the growth and exchange series upon injection of the cores into the mixture of Cd ions and phosphonic acids (cf. Figure 5a,b), leading to less non-radiative components and thus longer fluorescence lifetimes. Comparing the fluorescence decay curves of all aliquots with each other, it is noticeable that they are similar overall, and only in the growth series, the decay curves of the aliquots extracted after reaction times of 60 and 120 s reveal a considerably faster decay.

All fluorescence decay curves of the aliquots are strongly multi-exponential. A detailed analysis of the exact decay behavior is beyond the scope of this work. Here, we use a weighted average fluorescence lifetime as described in the Supporting Information to better compare the different decay dynamics.

Figure 8e shows the average fluorescence lifetime versus the sample number. Comparing the growth and the exchange series, differences in the lifetimes occur for reaction times of 60 and 120 s, where the lifetime significantly drops. The thin CdS shell leads to type-II band alignment with quasi-type-II behavior, in which the electron is delocalized over the whole particle. The decrease of the PL lifetime was reproducible between different, independent syntheses.

This behavior again suggests that the reaction processes in both sample series are similar for short reaction times, before the CdS shell growth starts at about 60 s of reaction time in the growth series. It is difficult to unambiguously assign the shortening of the average lifetime to its underlying physics. The decay curve reveals that fast processes lose their impact while medium-fast processes get faster and more dominant (cf. Table S3 for individual amplitudes and decay times). For the growth series, reaction times of 240 and 480 s lead to an increase of the average lifetime. This increase can be explained by an effective spatial charge carrier separation in the type-II heteronanostructure, with the hole trapped in the core and the electron localized within the elongated shell (cf. Figure 5e).

Figure 8f shows the fluorescence QY versus the sample number for the above discussed pair of sample series. Details of the experiments can be found in the Experimental section. The QY increases from below 1% for ZnSe cores to 7% after 10 s of reaction time in both the growth and the exchange series, which corresponds to less non-radiative decays compared to ZnSe cores. It increases further with increasing reaction time for the growth series, reaching a maximum of about 35% for the 60 s sample before decreasing again. The exchange series does not exhibit a strong change in the QY. Comparing both series, again, similar behaviors at small reaction times and significant differences after about 60 s of reaction time can be seen, the latter of which can be explained by the formation of a shell in the growth series.

Remarkably, the maximum of the QY is already reached after 60 s of reaction time for the growth series, which coincides with the shortest average fluorescence lifetime. This can be rationalized by a suppression of fast non-radiative decay channels, but it also shows the complexity of underlying exciton dynamics. The decreasing QY for very long reaction times in the growth series can be explained by additional non-radiative decay channels introduced by an increasing surface area of the growing shell.[3] At the same time, the average PL lifetime increases, which might be explained by slow radiative decay channels due to the low wave function overlap because of the type-II band alignment. Long fluorescence lifetimes might also be explained by hole trapping after excitation at the large rod's surface, which also leads to a low wave function overlap.[21]

CONCLUSIONS

In summary, we conducted a detailed study on the growth of an anisotropic CdS shell on spherical ZnSe-core nanocrystals. We performed TEM and linear and time-resolved absorption and PL spectroscopy analyses on aliquots taken during the synthesis as well as elemental analysis of a final dot-in-rod sample. The data were compared to results of a control experiment, in which the cadmium precursor but no sulfur was present during synthesis. In the control experiment, only cation exchange from ZnSe to $Zn_{1-x}Cd_xSe$ and no shell growth can occur.

We found that the CdS shell growth is slow at early stages of the reaction. By comparing linear optical spectra of the growth and exchange series, it was proven that cation exchange is the dominant process in the beginning of the reaction even when the shell precursors are present. Before significant CdS shell growth starts, about 50% of the initial Zn ions in the core are exchanged by Cd ions, which was determined by elemental analysis as well as a combination of PL spectroscopy and theoretical calculations. Anisotropic growth of the CdS shell starts not before 120 s of reaction time. Modeling of a dot-in-rod heterostructure with an alloyed $Zn_{1-x}Cd_xSe$ core showed a type-II band alignment with separated charge carriers.

Time-resolved optical measurements on the sample series fully support these findings. Increased rise times of the ground-state excitonic bleach measured in TA spectroscopy can be assigned to the formation of a type-II band alignment due to the development of the shell. A strong increase of the TA lifetime can be rationalized by the transition from spherical to rod-shaped shell growth, while a subsequent slight decrease in the lifetime can be attributed to charge carrier trapping, which becomes more important for larger shells. Drastic changes in the TA and fluorescence lifetimes in the very beginning of the syntheses is assigned to surface modifications. A decrease in the fluorescence lifetime, which coincides with the maximum PL QY, can be attributed to the full passivation of the core's surface by a complete CdS shell.

These findings highlight that cation exchange is inevitable in high-temperature reactions as used for rod growth on cores. This changes the band gap of the particles in the beginning and thus the band structure of the final particles. The reaction, usually referred to as the growth reaction, is an exchange of cations at early stages. The results can be transferred to other material combinations in which different cations and anions in

https://doi.org/10.1021/acs.chemmater.2c03278
Chem. Mater. 2023, 35, 1238−1248

the core and shell are present. Changes in the band alignment because of cation exchange must be considered if optoelectronic properties of the heterostructure are explained based on their band structure. Tuning the degree of cation exchange and thus the extent of the band offset could be used to selectively adjust the optical properties of the heterostructure.

EXPERIMENTAL SECTION

All chemicals were used as received. ODA (≥99%), trioctylphosphine oxide (TOPO, 99%), sulfur powder (S, 99.98%), and diethylzinc ($ZnEt_2$, 1.0 M in hexane) were purchased from Sigma-Aldrich; selenium (Se, 99.5% powder mesh 200) was purchased from Acros Organics; and TOP (97%) was purchased from ABCR. Cadmium oxide (CdO, 99.9999%) was purchased from ChemPur; ODPA (>99%) and HPA (>99%) were purchased from PCI Synthesis. Toluene (≥99.5%) was purchased from VWR, and methanol (99.5%) was purchased from Grüssing.

ZnSe core synthesis was adapted from Cozzoli et al.[58] Briefly, 7 g of ODA was degassed at 130 °C under vacuum. At 300 °C under a nitrogen flow, a mixture of 0.8 mL (1 M in hexane) of diethylzinc and 2.4 mL (0.33 M) of Se/TOP was injected, and the temperature was set to 265 °C. After 30 min, small ZnSe particles were formed, and further growth was achieved by adding 1 mL of the precursor solution within 5 min via a syringe pump followed by 30 min of reaction time. This cycle was repeated in total six times. The particles were cleaned by toluene/methanol extraction and centrifugation at 40 °C to avoid precipitation of ODA. Particles were stored in TOP in the glovebox.

The size was determined from the position of the first excitonic maximum, and the concentration was determined using size-dependent extinction coefficients from the literature.[38]

Anisotropic CdS shell growth was performed based on a method of Dorfs et al.[14] 3 g of TOPO, 290 mg of ODPA, 80 mg of HPA, and 60 mg of CdO were degassed at 150 °C under vacuum for 90 min and heated to 320 °C until it became optically clear and colorless. A mixture of 1.8 mL (2 M) of S/TOP and ZnSe cores (4×10^{-8} mol) was rapidly injected. For the exchange control experiment, S/TOP was replaced by TOP. Samples were extracted using a syringe into cold toluene at different time steps and purified by toluene/methanol extraction and centrifugation at 11,000 rpm, 10 min. This cycle was repeated three times.

Absorbance spectra were recorded on a Varian Cary 5000 UV/vis/NIR spectrometer in the wavelength range between 300 and 800 nm using quartz cuvettes with a 10 mm path length. The preparation was carried out by dispersing the aliquots in toluene.

PL spectra were recorded on a Horiba Yvon FluoroMax 4 by excitation of the aliquots in quartz cuvettes with energies above the first absorbance maximum.

QYs were calculated in relation to the organic dye Coumarin 153. The samples were excited at the intersection of the absorbance spectra of the dye and sample.

Fluorescence lifetime measurements were performed using a PicoQuant FluoTime FT300 equipped with a NKT SuperK Fianium white light laser source. Samples were excited above the CdS band gap. The detection wavelength was set to the maximum of the PL spectrum with a 2.7 nm bandwidth, and repetition rates of 3.7 MHz for ZnSe cores and 0.59 MHz for all aliquots were used.

A quantitative elemental analysis of the final dot-in-rod sample was performed by ICP−MS on an Agilent Technologies series 7700. For the preparation, the samples were placed in a vial, the toluene was evaporated, and the resulting precipitate was dissolved in aqua regia {[3:1 (v/v)] HCl/HNO_3} under stirring. After 16 h, the dissolved samples were diluted with 2% HCl.

TA spectroscopy was performed using an amplified Ti−sapphire laser (Spitfire-Ace, 800 nm, 1 kHz, 35 fs) as an excitation source seeding an optical parametric amplifier (TOPAS-Prime; Light Conversion) with a frequency mixer (NirUVis; Light Conversion) to reach the desired pump wavelength of 330 ± 20 nm using a constant power of 300. Each sample was measured using a broadband white-light continuum with a spectral range of 310−900 nm generated by a 2 mm thick sapphire crystal. The diameter of the pump beam covers around 500 μm, while the focused diameter of the probe beam is approximately 100 μm. The samples were diluted in toluene and filled in 2 mm thick quartz cuvettes (Hellma Analytics). A more detailed description of the TA setup can be found in the work of Minutella et al.[59]

The quantum mechanical calculations for the exciton energies of the $Zn_{1-x}Cd_xSe$ dots were carried out within the effective mass approximation based on the procedure reported by Panfil et al.[35,36] All equations were solved numerically using the software COMSOL Multiphysics based on the finite element method. Further details can be found in the Supporting Information.

ASSOCIATED CONTENT

Supporting Information

The Supporting Information is available free of charge at https://pubs.acs.org/doi/10.1021/acs.chemmater.2c03278.

Details of the calculation for spherical particles and heterostructures, absorbance and PL spectra of the second sample set, details of the fitting procedure for the PL lifetime, individual decay times and amplitudes of the fit of the PL decay curves, and details of the fitting procedure for TA spectra (PDF)

AUTHOR INFORMATION

Corresponding Authors

Alf Mews − *Institute of Physical Chemistry, University of Hamburg, 20146 Hamburg, Germany;* orcid.org/0000-0001-5739-8820; Email: mews@chemie.uni-hamburg.de

Tobias Kipp − *Institute of Physical Chemistry, University of Hamburg, 20146 Hamburg, Germany;* orcid.org/0000-0002-9663-7422; Email: kipp@chemie.uni-hamburg.de

Authors

Jannik Rebmann − *Institute of Physical Chemistry, University of Hamburg, 20146 Hamburg, Germany*

Hans Werners − *Institute of Physical Chemistry, University of Hamburg, 20146 Hamburg, Germany*

Florian Johst − *Institute of Physical Chemistry, University of Hamburg, 20146 Hamburg, Germany;* orcid.org/0000-0002-7594-8440

Marcel Dohrmann − *Institute of Physical Chemistry, University of Hamburg, 20146 Hamburg, Germany*

Yannic U. Staechelin − *Institute of Physical Chemistry, University of Hamburg, 20146 Hamburg, Germany;* orcid.org/0000-0001-8588-9117

Christian Strelow − *Institute of Physical Chemistry, University of Hamburg, 20146 Hamburg, Germany;* orcid.org/0000-0002-5989-1675

Complete contact information is available at: https://pubs.acs.org/10.1021/acs.chemmater.2c03278

Author Contributions

J.R., H.W., and A.M. conceived and designed the project. A.M. and T.K. supervised the project. J.R. synthesized and prepared all samples and performed TEM imaging and analysis and UV/vis absorption spectroscopy and (time-resolved) PL spectroscopy. H.W. performed all TA experiments (with the help of Y.U.S.), as well as analyzed and interpreted the TA data. F.J. performed the calculations (with the help of M.D. and C.S.). J.R., H.W., and T.K. prepared the manuscript with contributions from all co-authors.

https://doi.org/10.1021/acs.chemmater.2c03278
Chem. Mater. 2023, 35, 1238−1248

Notes

The authors declare no competing financial interest.

■ ACKNOWLEDGMENTS

The authors thank Stefan Werner for TEM images, Yang Liu for ICP−MS, and Holger Lange for support with TA measurements. The authors thank the Deutsche Forschungsgemeinschaft (DFG, German Research Foundation) for financial support via the Research Training Group "Nanohybrid" (GRK 2536). H.W. acknowledges the financial support by the Horizon-2020 research and innovation program of the European Union (grant no. 952335, NanoQIQO project).

■ REFERENCES

(1) García-Santamaría, F.; Chen, Y.; Vela, J.; Schaller, R. D.; Hollingsworth, J. A.; Klimov, V. I. Suppressed auger recombination in "Giant" nanocrystals boosts optical gain performance. *Nano Lett.* **2009**, *9*, 3482−8.

(2) Acharya, K. P.; Nguyen, H. M.; Paulite, M.; Piryatinski, A.; Zhang, J.; Casson, J. L.; Xu, H.; Htoon, H.; Hollingsworth, J. A. Elucidation of Two Giants: Challenges to Thick-Shell Synthesis in CdSe/ZnSe and ZnSe/CdS Core/Shell Quantum Dots. *J. Am. Chem. Soc.* **2015**, *137*, 3755−3758.

(3) Hinsch, A.; Lohmann, S. H.; Strelow, C.; Kipp, T.; Würth, C.; Geißler, D.; Kornowski, A.; Wolter, C.; Weller, H.; Resch-Genger, U.; Mews, A. Fluorescence Quantum Yield and Single-Particle Emission of CdSe Dot/CdS Rod Nanocrystals. *J. Phys. Chem. C* **2019**, *123*, 24338−24346.

(4) Klimov, V. I.; Mikhailovsky, A. A.; Xu, S.; Malko, A.; Hollingsworth, J. A.; Leatherdale, C. A.; Eisler, H.-J.; Bawendi, M. G. Optical Gain and Stimulated Emission in Nanocrystal Quantum Dots. *Science* **2000**, *290*, 314−317.

(5) Cunningham, P. D.; Souza, J. B.; Fedin, I.; She, C.; Lee, B.; Talapin, D. V. Assessment of Anisotropic Semiconductor Nanorod and Nanoplatelet Heterostructures with Polarized Emission for Liquid Crystal Display Technology. *ACS Nano* **2016**, *10*, 5769−5781.

(6) Kim, T.; Kim, K. H.; Kim, S.; Choi, S. M.; Jang, H.; Seo, H. K.; Lee, H.; Chung, D. Y.; Jang, E. Efficient and stable blue quantum dot light-emitting diode. *Nature* **2020**, *586*, 385−389.

(7) Shu, Y.; Lin, X.; Qin, H.; Hu, Z.; Jin, Y.; Peng, X. Quantum Dots for Display Applications. *Angew. Chem., Int. Ed.* **2020**, *59*, 22312−22323.

(8) Reiss, P.; Protière, M.; Li, L. Core/Shell Semiconductor Nanocrystals. *Small* **2009**, *5*, 154−168.

(9) Hines, M. A.; Guyot-Sionnest, P. Synthesis and Characterization of Strongly Luminescing ZnS-Capped CdSe Nanocrystals. *The Journal of Physical Chemistry* **1996**, *100*, 468−471.

(10) Xie, R.; Kolb, U.; Li, J.; Basché, T.; Mews, A. Synthesis and Characterization of Highly Luminescent CdSe-Core CdS/Zn 0.5 Cd 0.5 S/ZnS Multishell Nanocrystals. *J. Am. Chem. Soc.* **2005**, *127*, 7480−7488.

(11) Nemchinov, A.; Kirsanova, M.; Hewa-Kasakarage, N. N.; Zamkov, M. Synthesis and Characterization of Type II ZnSe/CdS Core/Shell Nanocrystals. *The Journal of Physical Chemistry C* **2008**, *112*, 9301−9307.

(12) de Mello Donegá, C. Formation of nanoscale spatially indirect excitons: Evolution of the type-II optical character of CdTe/CdSe heteronanocrystals. *Phys. Rev. B* **2010**, *81*, 165303.

(13) Lo, S. S.; Mirkovic, T.; Chuang, C.-H.; Burda, C.; Scholes, G. D. Emergent Properties Resulting from Type-II Band Alignment in Semiconductor Nanoheterostructures. *Adv. Mater.* **2011**, *23*, 180−197.

(14) Dorfs, D.; Salant, A.; Popov, I.; Banin, U. ZnSe quantum dots within CdS nanorods: A seeded-growth type-II system. *Small* **2008**, *4*, 1319−1323.

(15) Acharya, K. P.; Khnayzer, R. S.; O'Connor, T.; Diederich, G.; Kirsanova, M.; Klinkova, A.; Roth, D.; Kinder, E.; Imboden, M.; Zamkov, M. The role of hole localization in sacrificial hydrogen production by semiconductor-metal heterostructured nanocrystals. *Nano Lett.* **2011**, *11*, 2919−2926.

(16) Hewa-Kasakarage, N. N.; Kirsanova, M.; Nemchinov, A.; Schmall, N.; El-Khoury, P. Z.; Tarnovsky, A. N.; Zamkov, M. Radiative recombination of spatially extended excitons in (ZnSe/CdS)/CdS heterostructured nanorods. *J. Am. Chem. Soc.* **2009**, *131*, 1328−1334.

(17) Kuo, Y.; Li, J.; Michalet, X.; Chizhik, A.; Meir, N.; Bar-Elli, O.; Chan, E.; Oron, D.; Enderlein, J.; Weiss, S. Characterizing the Quantum-Confined Stark Effect in Semiconductor Quantum Dots and Nanorods for Single-Molecule Electrophysiology. *ACS Photonics* **2018**, *5*, 4788−4800.

(18) Bar-Elli, O.; Steinitz, D.; Yang, G.; Tenne, R.; Ludwig, A.; Kuo, Y.; Triller, A.; Weiss, S.; Oron, D. Rapid Voltage Sensing with Single Nanorods via the Quantum Confined Stark Effect. *ACS Photonics* **2018**, *5*, 2860−2867.

(19) Ghosh, S.; Chizhik, A. M.; Yang, G.; Karedla, N.; Gregor, I.; Oron, D.; Weiss, S.; Enderlein, J.; Chizhik, A. I. Excitation and Emission Transition Dipoles of Type-II Semiconductor Nanorods. *Nano Lett.* **2019**, *19*, 1695−1700.

(20) O'Connor, T.; Panov, M. S.; Mereshchenko, A.; Tarnovsky, A. N.; Lorek, R.; Perera, D.; Diederich, G.; Lambright, S.; Moroz, P.; Zamkov, M. The effect of the charge-separating interface on exciton dynamics in photocatalytic colloidal heteronanocrystals. *ACS Nano* **2012**, *6*, 8156−65.

(21) Grennell, A. N.; Utterback, J. K.; Pearce, O. M.; Wilker, M. B.; Dukovic, G. Relationships between Exciton Dissociation and Slow Recombination within ZnSe/CdS and CdSe/CdS Dot-in-Rod Heterostructures. *Nano Lett.* **2017**, *17*, 3764−3774.

(22) Boldt, K.; Schwarz, K. N.; Kirkwood, N.; Smith, T. A.; Mulvaney, P. Electronic structure engineering in ZnSe/CdS type-II nanoparticles by interface alloying. *J. Phys. Chem. C* **2014**, *118*, 13276−13284.

(23) Boldt, K.; Bartlett, S.; Kirkwood, N.; Johannessen, B. Quantification of Material Gradients in Core/Shell Nanocrystals Using EXAFS Spectroscopy. *Nano Lett.* **2020**, *20*, 1009−1017.

(24) Huang, J.; Kovalenko, M. V.; Talapin, D. V. Alkyl chains of surface ligands affect polytypism of CdSe nanocrystals and play an important role in the synthesis of anisotropic nanoheterostructures. *J. Am. Chem. Soc.* **2010**, *132*, 15866−15868.

(25) Hewa-Kasakarage, N. N.; El-Khoury, P. Z.; Tarnovsky, A. N.; Kirsanova, M.; Nemitz, I.; Nemchinov, A.; Zamkov, M. Ultrafast carrier dynamics in type II ZnSe/CdS/ZnSe nanobarbells. *ACS Nano* **2010**, *4*, 1837−1844.

(26) Groeneveld, E.; Witteman, L.; Lefferts, M.; Ke, X.; Bals, S.; Van Tendeloo, G.; de Mello Donega, C. Tailoring ZnSe-CdSe colloidal quantum dots via Cation Exchange: From core/shell to alloy nanocrystals. *ACS Nano* **2013**, *7*, 7913−7930.

(27) Lee, S.; Yoon, D. E.; Kim, D.; Shin, D. J.; Jeong, B. G.; Lee, D.; Lim, J.; Bae, W. K.; Lim, H. K.; Lee, D. C. Direct cation exchange of CdSe nanocrystals into ZnSe enabled by controlled binding between guest cations and organic ligands. *Nanoscale* **2019**, *11*, 15072−15082.

(28) Ohtani, H.; Kojima, K.; Ishida, K.; Nishizawa, T. Miscibility gap in II-VI alloy semiconductor systems. *J. Alloys Compd.* **1992**, *182*, 103−114.

(29) Steiner, D.; Dorfs, D.; Banin, U.; Della Sala, F. D.; Manna, L.; Millo, O. Determination of band offsets in heterostructured colloidal nanorods using scanning tunneling spectroscopy. *Nano Lett.* **2008**, *8*, 2954−2958.

(30) Cao, G.; Lynch, V. M.; Yacullo, L. N. Synthesis, Structural Characterization, and Intercalation Chemistry of Two Layered Cadmium Organophosphonates. *Chem. Mater.* **1993**, *5*, 1000−1006.

(31) García-Rodríguez, R.; Hendricks, M. P.; Cossairt, B. M.; Liu, H.; Owen, J. S. Conversion reactions of cadmium chalcogenide nanocrystal precursors. *Chem. Mater.* **2013**, *25*, 1233−1249.

(32) Qiao, F.; Xu, W.; Liu, M.; Yang, J.; Cui, X.; Wang, Q.; Bian, J.; Kim, D. H. Effect of Cd-phosphonate complex on the self-assembly structure of colloidal nanorods. *Mater. Lett.* **2016**, *180*, 85−88.

https://doi.org/10.1021/acs.chemmater.2c03278
Chem. Mater. 2023, 35, 1238−1248

(33) Wang, W.; Banerjee, S.; Jia, S.; Steigerwald, M. L.; Herman, I. P. Ligand control of growth, morphology, and capping structure of colloidal CdSe nanorods. *Chem. Mater.* **2007**, *19*, 2573−2580.
(34) Fischli, D.; Enders, F.; Boldt, K. Kinetically Driven Cadmium Chalcogenide Nanorod Growth Fed by Local Cluster Aggregates. *J. Phys. Chem. C* **2020**, *124*, 12774−12783.
(35) Panfil, Y. E.; Shamalia, D.; Cui, J.; Koley, S.; Banin, U. Electronic coupling in colloidal quantum dot molecules; the case of CdSe/CdS core/shell homodimers. *J. Chem. Phys.* **2019**, *151*. DOI: 10.1063/1.5128086
(36) Panfil, Y. E.; Cui, J.; Koley, S.; Banin, U. Complete Mapping of Interacting Charging States in Single Coupled Colloidal Quantum Dot Molecules. *ACS Nano* **2022**, *16*, 5566−5576.
(37) Zhong, X.; Feng, Y.; Zhang, Y.; Gu, Z.; Zou, L. A facile route to violet- to orange-emitting Cd x Zn 1- x Se alloy nanocrystals via cation exchange reaction. *Nanotechnology* **2007**, *18*, 385606.
(38) Toufanian, R.; Zhong, X.; Kays, J. C.; Saeboe, A. M.; Dennis, A. M. Correlating ZnSe Quantum Dot Absorption with Particle Size and Concentration. *Chem. Mater.* **2021**, *33*, 7527−7536.
(39) Reiss, P. ZnSe based colloidal nanocrystals: Synthesis, shape control, core/shell, alloy and doped systems. *New J. Chem.* **2007**, *31*, 1843−1852.
(40) de Mello Donegá, C. Synthesis and properties of colloidal heteronanocrystals. *Chem. Soc. Rev.* **2011**, *40*, 1512−1546.
(41) Puzder, A.; Williamson, A. J.; Zaitseva, N.; Galli, G.; Manna, L.; Alivisatos, A. P. The Effect of Organic Ligand Binding on the Growth of CdSe Nanoparticles Probed by Ab Initio Calculations. *Nano Lett.* **2004**, *4*, 2361−2365.
(42) Adachi, S. *Paper Knowledge. Toward a Media History of Documents*; John Wiley & Sons, Ltd, 2015; p 406.
(43) Wei, S. H.; Zunger, A. Calculated natural band offsets of all II-VI and III-V semiconductors: Chemical trends and the role of cation d orbitals. *Appl. Phys. Lett.* **1998**, *72*, 2011−2013.
(44) Ekvall, K.; van der Meulen, P.; Dhollande, C.; Berg, L. E.; Pommeret, S.; Naskrecki, R.; Mialocq, J. C. Cross phase modulation artifact in liquid phase transient absorption spectroscopy. *J. Appl. Phys.* **2000**, *87*, 2340−2352.
(45) El-Ballouli, A. O.; Alarousu, E.; Usman, A.; Pan, J.; Bakr, O. M.; Mohammed, O. F. Real-Time Observation of Ultrafast Intraband Relaxation and Exciton Multiplication in PbS Quantum Dots. *ACS Photonics* **2014**, *1*, 285−292.
(46) Guyot-Sionnest, P.; Wehrenberg, B.; Yu, D. Intraband relaxation in CdSe nanocrystals and the strong influence of the surface ligands. *J. Chem. Phys.* **2005**, *123*. DOI: 10.1063/1.2004818
(47) Kambhampati, P. Hot exciton relaxation dynamics in semiconductor quantum dots: Radiationless transitions on the nanoscale. *J. Phys. Chem. C* **2011**, *115*, 22089−22109.
(48) Klimov, V. I.; Mikhailovsky, A. A.; McBranch, D. W.; Leatherdale, C. A.; Bawendi, M. G. Quantization of multiparticle Auger rates in semiconductor quantum dots. *Science* **2000**, *287*, 1011−1013.
(49) Klimov, V. I. Spectral and dynamical properties of multiexcitons in semiconductor nanocrystals. *Annu. Rev. Phys. Chem.* **2007**, *58*, 635−673.
(50) Califano, M.; Zunger, A.; Franceschetti, A. Direct carrier multiplication due to inverse auger scattering in CdSe quantum dots. *Appl. Phys. Lett.* **2004**, *84*, 2409−2411.
(51) Schaller, R. D.; Klimov, V. I. High efficiency carrier multiplication in PbSe nanocrystals: Implications for solar energy conversion. *Phys. Rev. Lett.* **2004**, *92*, 1−4.
(52) Xing, G.; Liao, Y.; Wu, X.; Chakrabortty, S.; Liu, X.; Yeow, E. K. L.; Chan, Y.; Sum, T. C. Ultralow-Threshold Two-Photon Pumped Amplified Spontaneous Emission and Lasing from Seeded CdSe/CdS Nanorod Heterostructures. *ACS Nano* **2022**, *6*, 10835−10844.
(53) Achtstein, A. W.; Hennig, J.; Prudnikau, A.; Artemyev, M. V.; Woggon, U. Linear and Two-Photon Absorption in Zero- and One-Dimensional CdS Nanocrystals: In fluence of Size and Shape. *J. Phys. Chem. C* **2013**, *117*, 25756−25760.
(54) Morgan, D. P.; Kelley, D. F. What Does the Transient Absorption Spectrum of CdSe Quantum Dots Measure? *J. Phys. Chem. C* **2020**, *124*, 8448−8455.
(55) Cohn, A. W.; Schimpf, A. M.; Gunthardt, C. E.; Gamelin, D. R. Size-dependent trap-assisted auger recombination in semiconductor nanocrystals. *Nano Lett.* **2013**, *13*, 1810−1815.
(56) Tyagi, P.; Kambhampati, P. False multiple exciton recombination and multiple exciton generation signals in semiconductor quantum dots arise from surface charge trapping. *J. Chem. Phys.* **2011**, *134*. DOI: 10.1063/1.3561063
(57) Klimov, V. I. Optical nonlinearities and ultrafast carrier dynamics in semiconductor nanocrystals. *J. Phys. Chem. B* **2000**, *104*, 6112−6123.
(58) Cozzoli, P. D.; Manna, L.; Curri, M. L.; Kudera, S.; Giannini, C.; Striccoli, M.; Agostiano, A. Shape and phase control of colloidal ZnSe nanocrystals. *Chem. Mater.* **2005**, *17*, 1296−1306.
(59) Minutella, E.; Schulz, F.; Lange, H. Excitation-dependence of plasmon-induced hot electrons in gold nanoparticles. *J. Phys. Chem. Lett.* **2017**, *8*, 4925−4929.

https://doi.org/10.1021/acs.chemmater.2c03278
Chem. Mater. 2023, 35, 1238−1248